Spin–orbit-resolved spectral phase measurements around a Fano resonance

M. Turconi, L. Barreau, D Busto, M. Isinger, C Alexandridi, A Harth, R. J
Squibb, D Kroon, C. Arnold, R. Feifel, et al.

Spin-orbit-resolved spectral phase measurements around a Fano resonance

M Turconi[1], L Barreau[1], D Busto[2], M Isinger[2], C Alexandridi[1], A Harth[2] , R J Squibb[3], D Kroon[2], C L Arnold[2], R Feifel[3], M Gisselbrecht[2], L Argenti[4], F Martín[5,6,7], A L 'Huillier[2] and P Salières[1]

[1]Université Paris-Saclay, CEA, CNRS, LIDYL, 91191 Gif-sur-Yvette, France
[2]Department of Physics, Lund University, P.O. Box 118, SE-221 00 Lund, Sweden
[3]Department of Physics, University of Gothenburg, Origovägen 6B, SE-41296 Gothenburg, Sweden
[4]Department of Physics & CREOL, University of Central Florida, FL 32816, United States of America
[5]Departamento de Química, Módulo 13, Universidad Autónoma de Madrid, E-28049 Madrid, Spain
[6]Instituto Madrileño de Estudios Avanzados en Nanociencia (IMDEA-Nanociencia), Cantoblanco,E-28049 Madrid, Spain
[7]Condensed Matter Physics Center (IFIMAC), Universidad Autnoma de Madrid, E-28049 Madrid, Spain

E-mail: `pascal.salieres@cea.fr`

Abstract. We apply a spectrally-resolved electron interferometry technique to the measurement of the spectral phase in the vicinity of the $3s^1 3p^6 4p$ Fano resonance of argon. We show that it allows disentangling the phases of the two nearly-overlapping electron wavepackets corresponding to different spin-orbit final states. Using simple assumptions, it is possible to process the experimental data and numerically isolate each component in a self-consistent manner. This in turn allows reconstructing the autoionization dynamics of the dominant channel.

1. Introduction

The advent of attosecond spectroscopy has allowed the investigation of fundamental processes such as photoionization on their natural timescale [1]. In particular, it is now possible to measure attosecond delays between electron wave packets (EWP) emitted from different electronic shells of atoms [2, 3, 4, 5], molecules [6, 7, 8, 9, 10, 11] and solids [12, 13, 14] (see [15, 16, 17] for reviews on theory and experiments). These attosecond delays can be accessed by different methods: either directly in the time domain using the attosecond streaking technique [18, 19], or through the measurement of the spectral variation of the scattering phase using the RABBIT (Reconstruction of Attosecond Beating By Interference of two-photon Transitions) technique [20, 21].

Recently, two particularly challenging cases have been investigated. On the one hand, the influence of the atomic fine structure on photoionization time delays was studied by Jordan *et al.* [22]. Up to 33-as delays were measured in xenon between EWPs originating from the same electronic shell but leaving the ion in different spin-orbit (S-O) configurations, whereas very small (< 8 as) delays were measured between the two S-O components of krypton. This demonstrated that relativistic effects may influence photoionization time delays. Important effects are expected in systems involving heavy elements, in molecules and solids.

On the other hand, studies have been conducted in the vicinity of autoionizing resonances [23, 24, 25, 26, 27, 28, 29], a well-known example of the important role of electron correlation in light-matter interaction. The presence of autoionizing resonances is known since the measurement of unusual asymmetric peak shapes in the absorption of noble gases [30]. Fano explained this phenomenon as the interference between direct photoionization and photoexcitation to a discrete state coupled to the final continuum by configuration interaction [31]. Since then, Fano resonances have been intensively studied using synchrotron radiation, allowing very precise measurements of their energetic locations and cross sections (e.g. [32, 33] in argon). The possibility of measuring the phase of the Fano resonance transition amplitude (i.e. the spectral phase in the vicinity of the resonance) was demonstrated by Kotur *et al.* [24] in argon, however without resolving the spin-orbit components. Different RABBIT spectrograms were recorded as harmonic H17 was tuned across the resonance by controlling the laser driving wavelength. In Gruson *et al.* [25], the EWP emitted through the $2s2p$ Fano resonance in helium was fully characterized using spectrally-resolved RABBIT (Rainbow RABBIT), which allowed reconstructing the complete autoionization dynamics from a single spectrogram.

In this work, we go one step further compared to previous works [22, 24]. We measure the spectral phase across the $3s^13p^64p$ (hereafter denoted $3s^{-1}4p$) Fano resonance in argon for both S-O components by using the Rainbow RABBIT technique. The features are nearly-overlapping due to the comparatively small S-O splitting (177 meV [34]), but distinct signatures can be observed in the spectrally-resolved amplitude and phase near the resonance. We apply a numerical procedure, based on simple assumptions, that allows complete separation of the two S-O components. Our results compare well with the predictions of our theoretical model, giving access to the autoionization dynamics of the dominant channel. In section 2, we

describe the experiment, the analysis method and the experimental results. In section 3, we introduce the model used to simulate the spectral amplitude and phase retrieved from the Rainbow RABBIT technique. The comparison between the experimental and theoretical results is presented in section 4, together with the reconstruction of the autoionization dynamics. Finally, we draw conclusions in section 5.

2. Experimental Results

2.1. Experimental Setup

The experiment relies on the RABBIT electron interferometry technique, with a setup similar to the one used in [28]. It consists in ionizing argon atoms by a train of extreme ultra-violet (XUV) pulses in presence of a weak infrared (IR) pulse, and measuring the photoelectron spectrum as a function of the XUV-IR delay. The driving laser is a Ti:Sa system producing ∼800-nm 5-mJ 22-fs pulses at 1 kHz repetition rate. The laser beam is split in two: the generation beam and a weak dressing beam. The generation beam is focused in an argon gas cell to generate a train of XUV attosecond pulses, that corresponds to a comb of odd order harmonics of the fundamental laser frequency ω_0. A 200-nm thick Al filter blocks the remaining IR radiation and transmits the XUV pulses that are then recombined with the dressing beam and focused into the argon target gas jet for laser-assisted photoionization. The photoelectrons are detected by a magnetic bottle electron spectrometer (MBES), with a collection angle of 4π sr and a resolution better than 100 meV for electrons with kinetic energy $E_{kin} < 5$ eV. A retarding potential is applied in the MBES in order to shift the spectral
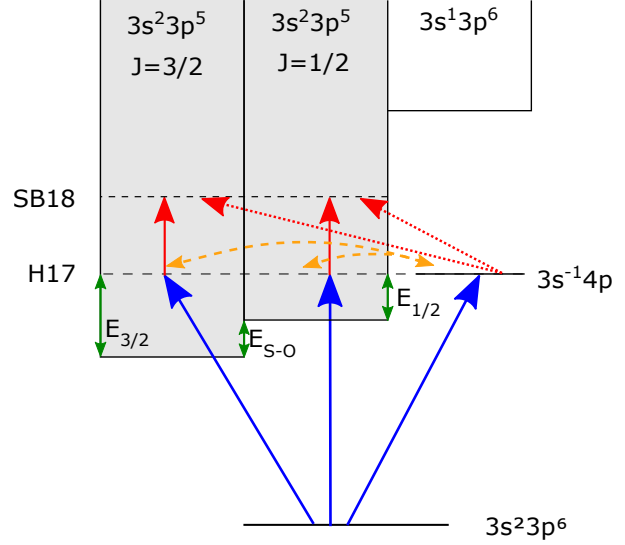

Figure 1: Schematic representation of the energy levels and transitions involved in this work. The blue (red) arrows represent absorption of an XUV (IR) photon. The orange dashed arrows represent the configuration interaction between the quasi-bound state $3s^{-1}4p$ and the continua. The processes indicated by the red dotted arrows stand for the dipole coupling of the $3s^{-1}4p$ state with the final continua through absorption of an IR photon. $E_{3/2}$ and $E_{1/2}$ are the kinetic energies of the electrons for different final states of the ion, separated by E_{S-O}.

region of interest to this low energy and thus reach the optimal resolution. Harmonic 17 (H17) has an energy close to the $3s^{-1}4p$ Fano resonance, located at $E_{res} = 26.6$ eV. Using a combination of two acousto-optical programmable dispersive filters (DAZZLER and MAZZLER) as in [24], the laser central wavelength can be tuned from 780 nm to 820 nm with a bandwidth of 50 nm (corresponding to ∼35-fs pulses), which allows tuning H17 across the resonance. A scheme of the resonant transition induced by H17 is represented in

figure 1 by blue arrows.

Figure 2 shows the XUV-only photoelectron spectra for different wavelengths of the driving laser. The photoelectron peak due to ionization with non-resonant H19 exhibits a double structure that simply shifts but remains essentially unchanged with wavelength. This is due to the overlapping S-O components that are only partially resolved due to both the harmonic bandwidth and the spectrometer resolution. In contrast, the shape of the peak coming from H17 changes dramatically when the energy of the resonant harmonic is varied. Its shape is governed both by the S-O splitting and the Fano resonance. For short wavelengths (λ = 785-788 nm), when H17 is tuned just above the resonance, the photoelectron spectrum shows a pronounced double structure that is mainly due to the S-O splitting. As the wavelength increases (λ = 789-792 nm), a three-peak structure appears. The intensity of each peak changes as the wavelength is varied while the global signal is lower (especially for λ = 790-791 nm). These modifications are the signature of the window resonance, as we will see later. Finally, for λ = 794 nm, H17 is just below the resonance and the lineshape is similar to the short wavelength case. The entire resonance has been scanned and its signature was visible in both S-O channels.

The dressing field is then spatially and temporally overlapped with the XUV in the MBES interaction region, inducing two-photon XUV+IR and XUV−IR transitions and leading to the formation of satellite peaks in the photoelectron spectrum (the so-called sidebands (SB), see figure 1). These sidebands encode the spectral interference between replicas of the two neighboring EWPs created by absorption of high-order harmonics. The spectral phase of the resonant H17 EWP
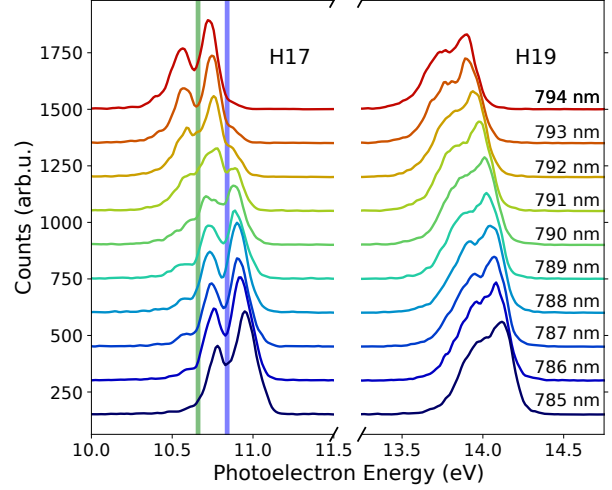

Figure 2: Photoelectron spectra for different wavelengths of the driving laser, from 785 to 794 nm. Spectra are shifted vertically for clarity, in decreasing laser wavelength from top to bottom in 1 nm step. The green and blue areas in harmonic 17 mark the position of the $3s^{-1}4p$ resonance, visible at different kinetic energies depending on the final state of the ion (E_{kin} = 10.66 eV for J = 1/2 and at E_{kin} = 10.84 eV for J = 3/2, see figure 1).

is thus encoded in SB16 and SB18, the non-resonant H15 and H19 EWPs serving as references. By recording the photoelectron spectrum as a function of the delay τ between the XUV and IR pulses, a RABBIT spectrogram is obtained. This delay is actively stabilized to correct for spatial and temporal jitters [35]. The high resolution of the MBES allows using the Rainbow RABBIT technique to extract the entire variation of the amplitude and phase across the sideband by analyzing the $2\omega_0$ oscillations as a function of energy, where ω_0 is the driving laser angular frequency [5, 9, 25, 28].

2.2. Numerical separation of the spin-orbit components

Due to the fine structure of argon, the measured photoelectron spectrum S^{tot} is the incoherent sum of two independent spectra corresponding to the $J = 1/2$ and $J = 3/2$ final states of Ar^+:

$$S^{tot}(E) = S^{1/2}(E) + S^{3/2}(E). \qquad (1)$$

Electrons corresponding to the $J = 3/2$ final state have a 177-meV higher kinetic energy than electrons corresponding to $J = 1/2$ [34]. Because of the spectral overlap of the two S-O components, the extraction of the spectral amplitude and phase by the Rainbow RABBIT technique is not straightforward.

To study the influence of the Fano resonance on the spectral phase and amplitude of the photoelectron wave-packet, it is necessary to disentangle the contribution of the two S-O components.

Our method takes advantage of the periodicity of the photoelectron spectrum to separating numerically the two S-O contributions by Fourier transformation [36]. We assume that the two S-O spectra are identical, shifted by the spin-orbit energy difference $E_{\text{S-O}}$ and scaled by the degeneracy of the $^2P_{1/2}$ and $^2P_{3/2}$ states of Ar^+. Thus the two spectra corresponding to the two S-O components can be written as:

$$S^{1/2}(E) = S(E) \text{ and } S^{3/2}(E) = 2S(E - E_{\text{S-O}}). \qquad (2)$$

Equation 1 for the measured photoelectron spectrum becomes:

$$S^{tot}(E) = S(E) + 2S(E - E_{\text{S-O}}) \qquad (3)$$

and its Fourier transform (FT), with η the transform variable of E:

$$\widetilde{S}^{tot}(\eta) = (1 + 2e^{-i\eta E_{\text{S-O}}})\widetilde{S}(\eta) \qquad (4)$$
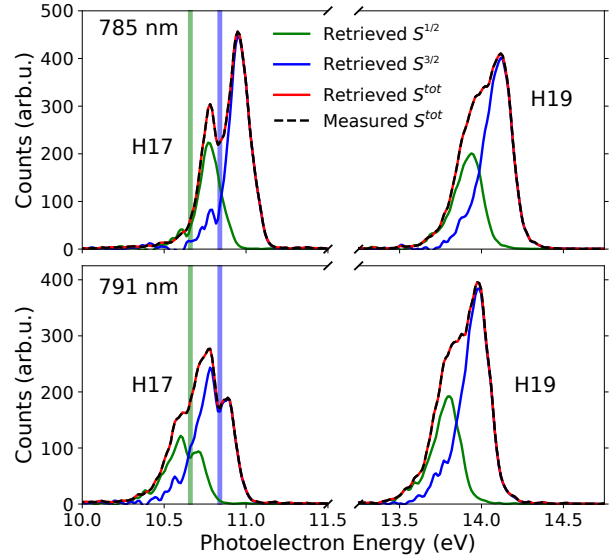

Figure 3: Retrieved (red line) and measured (black dashed line) XUV-only photoelectron spectra, for $\lambda = 785$ nm (upper panel) and $\lambda = 791$ nm (lower panel). The two S-O components $J = 1/2$ and $J = 3/2$ are shown in green and blue respectively. The total retrieved signal is in excellent agreement with the measured signal.

The expression for $S(E)$ can be obtained by inverse FT:

$$S(E) = \text{Re}\left[FT^{-1}\left(\frac{\widetilde{S}^{tot}(\eta)}{2e^{-i\eta E_{\text{S-O}}} + 1}\right)\right] \qquad (5)$$

The spectrum of each S-O ionization channel is then obtained by equation 2. As the energy calibration of the photoelectron spectrum may be imperfect, the value of $E_{\text{S-O}}$ is optimized by an algorithm which minimizes the difference between the experimentally measured spectrum and the one calculated by using equation 3. We first applied this procedure to the XUV-only photoelectron spectra shown in figure 2. The extracted value of 180 meV is in very good agreement with the literature values. The imaginary part of the inverse FT in equation 5 is

found to be negligible, indicating the validity of our assumptions. The total spectra, reconstructed from $S(E)$ using equation 3, are in excellent agreement with the measured ones, as illustrated in figure 3 for $\lambda = 785$ nm and $\lambda = 791$ nm. While the non-resonant harmonic H19 is bell-shaped for each S-O component (green and blue lines), the resonant harmonic H17 shows the imprint of the window resonance that digs a hole on the low-energy side for $\lambda = 785$ nm and around the maximum for $\lambda = 791$ nm. The latter case shows that the sum of the two resonant S-O components is responsible for the three peaks observed in the total spectrum S^{tot}. Remarkably, the ratio of the two S-O cross-sections, that can vary around 1.9 in the vicinity of the Fano resonances [37, 38], does not seem to be a critical parameter and our assumption of a constant value of 2 over the whole spectral range does not lead to significant discrepancies.

2.3. Resonant phase for the two spin-orbit components

We now apply this method to the RABBIT spectrogram obtained at $\lambda = 791$ nm and shown in figure 4(a). In order to isolate the contribution of a single S-O component, the procedure described in section 2.2 is applied to each spectrum at every delay. By doing this, we extend the assumptions made in section 2.2 from one-photon to two-photon transitions. The two retrieved RABBIT spectrograms, corresponding to the two S-O components, are shown in figures 4 (b)-(c). The total spectrogram is reconstructed by applying equation 3. The difference with the measured RABBIT spectrogram is negligible as seen in figure 4(d). Therefore the assumptions concerning the two S-O components in equation 2 lead to self-
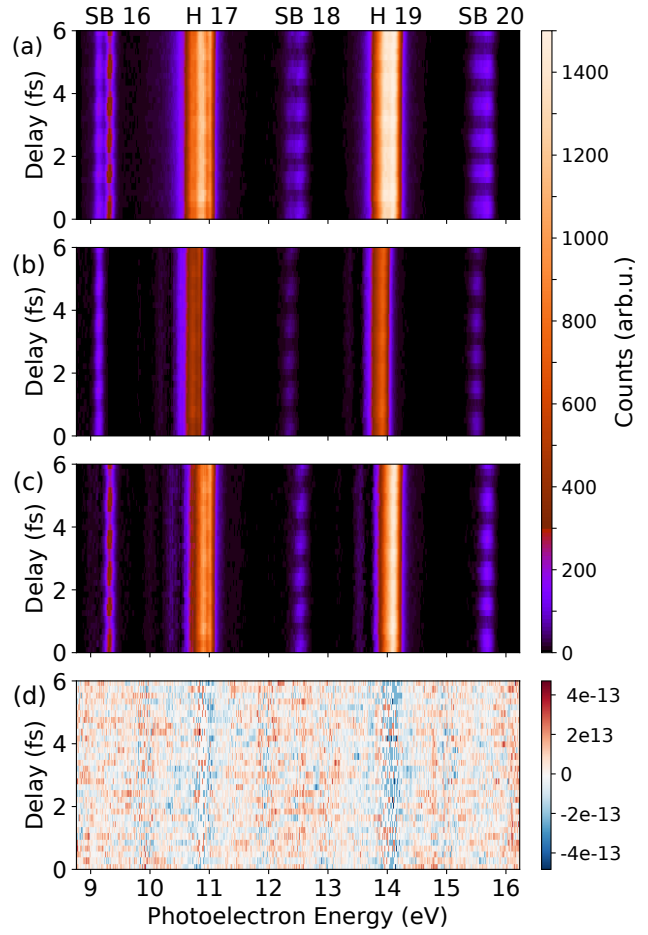

Figure 4: (a) Measured RABBIT spectrogram at $\lambda = 791$ nm; (b-c) retrieved RABBIT spectrograms for $J = 1/2$ (b) and for $J = 3/2$ (c). Differently scaled colormaps are used for sidebands and harmonics for the sake of better visibility. (d) Difference between the measured RABBIT spectrogram and the total retrieved one (d = a-(b+c)).

consistent results. Each spectrogram can then be analyzed with the Rainbow RABBIT method. The resulting spectral amplitudes and phases for the resonant sidebands SB16 and SB18 and the non-resonant SB20 are shown in figure 5. The amplitude and phase of the measured (black dashed line) and reconstructed total (red) spectrograms are in very good agreement with each other.
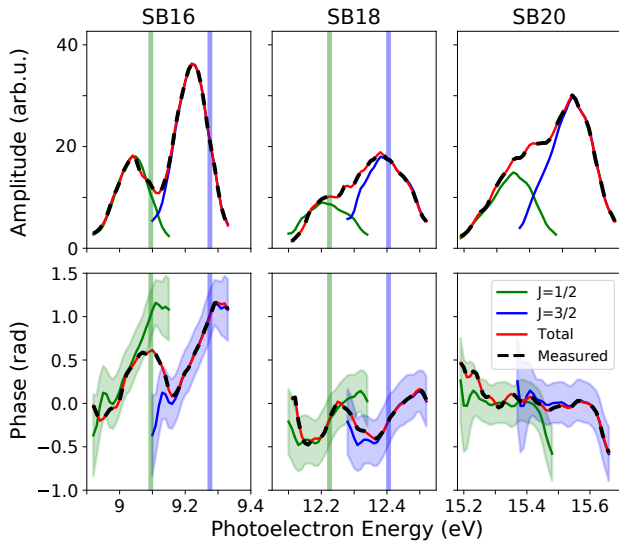
Figure 5: Experimentally measured spectral amplitudes and phases (black dashed lines) of the $2\omega_0$ component of SB16, SB18 and SB20, for $\lambda = 791$ nm. The amplitudes and phases of the two S-O components retrieved using the procedure detailed in the text are shown in green for $J = 1/2$, blue for $J = 3/2$ and red for the total. The shaded area around the spectral phases represent the error-bars. They are estimated as the statistical error from the FT phase-retrieval algorithm, normalized by the signal to noise ratio. The intrinsic group delay dispersion of the ionizing harmonic radiation, related to the attochirp [39], has been removed. The green and blue vertical lines indicate the positions of the resonance shifted up (SB18) or down (SB16) by the energy of one photon.

The double signature of the resonance is not clearly visible in the amplitudes (as it was in the XUV-only spectra of figure 3) but is clear in the phases. In contrast to the non-resonant SB20 phase that is rather flat, the measured phases for the resonant SBs show large spectral variations with double structures, a behavior markedly different from the experimental results of reference [24] which

were S-O averaged. This observation is made possible by the high spectral resolution of the Rainbow RABBIT technique.

These modulations can be related, although non-trivially, to that in each reconstructed S-O component. The corresponding phases (in green and blue lines) show, for both SB16 and SB18, a modulation across the energy value corresponding to the resonance shifted by the energy of one laser photon, $E_{res} \pm \hbar\omega_0$ (green and blue vertical lines). In contrast to what was observed in helium [25], the phase of the lower energy SB is not equal to the opposite of the phase of the higher energy SB. Here, the phase of SB16 increases monotonically from 0 to 1.2 rad before the resonance whereas the phase of SB18 first decreases from 0 to -0.5 rad, then is rather flat before increasing back to 0 at the resonance. The reason for this discrepancy will be clarified in section 4. Note that the numerical separation procedure intrinsically yields identical results for the two S-O components, apart from an energy shift and a scaling in the amplitude.

3. Simulations

In order to interpret the measured phases in terms of resonance-induced phases in the two spin-orbit components, we performed RABBIT simulations. To describe the resonance, we use the non-relativistic model of [24], assuming that relativistic effects are negligible so that the resonant two-photon transitions for the $J = 1/2$ and $J = 3/2$ components are identical, except for the scaling and spectral shift factors in equation 2. The total SB signal is proportional to the incoherent sum of transition probabilities towards different final states, characterized by the quantum numbers L (total orbital angular momentum) and ℓ (angular momentum of the

ionized electron). In the case of argon, there are three channels: $L = 0$ $\ell = 1$, $L = 2$ $\ell = 1$, and $L = 2$ $\ell = 3$. For each channel, we compute the intensity of the oscillating SB for the two S-O components as follows:

$$SB_{18,16}^{1/2,L,\ell}(\tau, E) = |A_{nr}(E)|^2 + \left|A_r^{\pm,L,\ell}(E)\right|^2 +$$

$$2|A_{nr}(E)|\left|A_r^{\pm,L,\ell}(E)\right|\cos\left(2\omega_0\tau \mp \Delta\Phi_a^{\pm,L,\ell}(E)\right),$$

$$SB_{18,16}^{3/2,L,\ell}(\tau, E) = 2\, SB_{18,16}^{1/2,L,\ell}(\tau, E - E_{\text{S-O}}), \quad (6)$$

where ω_0 stands for the driving laser angular frequency, τ for the XUV-IR delay, $A_{nr}(E)$ and $A_r^{\pm,L,\ell}(E)$ are the non-resonant and resonant two-photon transition amplitudes, and $\Delta\Phi_a^{\pm,L,\ell}$ is their phase difference. The symbol $(\pm)$ indicates whether the IR photon is absorbed $(+)$ or emitted $(-)$ for the resonant path; L, ℓ indicate the given channel. The resonant and non-resonant transition amplitudes can be written as a function of the harmonic spectral amplitude $\mathcal{H}$ and the resonant two-photon transition matrix element $\mathcal{M}_r^{\pm,L,\ell}$ as

$$A_{nr}(E) \propto \mathcal{H}(E), \quad (7)$$

$$A_r^{\pm,L,\ell}(E) \propto \mathcal{H}(E)\mathcal{M}_r^{\pm,L,\ell}(E). \quad (8)$$

The final intensities of the SBs are given by the sum over all channels and components convoluted with the MBES response function Sp:

$$SB_{18,16}(\tau, E) = Sp(E) *$$

$$\left[\sum_{L,\ell} SB_{18,16}^{1/2,L,\ell}(\tau, E) + \sum_{L,\ell} SB_{18,16}^{3/2,L,\ell}(\tau, E)\right] \quad (9)$$

In argon, the presence of two continua (s and d) to which the resonance is coupled by configuration interaction can be reduced to the case of an "interacting" and a "non-interacting" continua [31]. This results in the following expression for the one-photon absorption cross-section σ [40]:

$$\sigma(\varepsilon) = \sigma_a\frac{(q+\varepsilon)^2}{1+\varepsilon^2} + \sigma_b \quad (10)$$
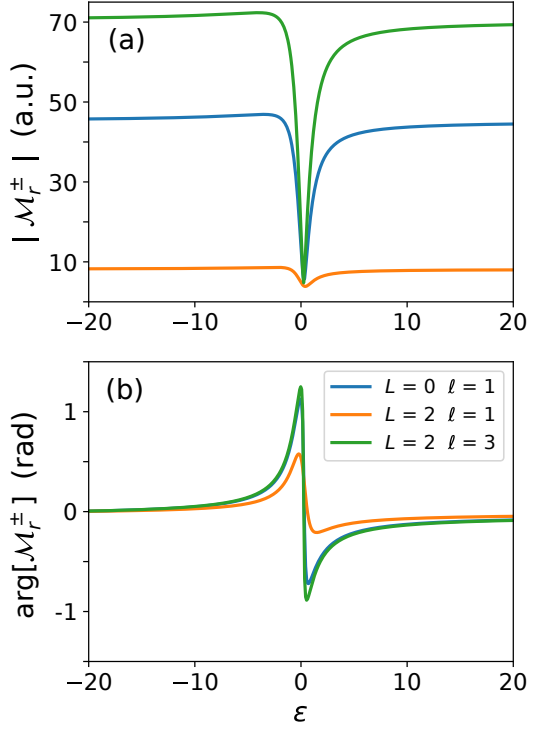

Figure 6: Modulus (a) and phase (b) of the two photon transition matrix elements with $\beta = 0$ ($q_{\text{eff}}^{\pm} = q$) as a function of the reduced energy, for the three channels. The phase curves have been shifted to 0 for $\epsilon \to \infty$.

where σ_b represents the (constant) non-interacting part, while σ_a is the off-resonant contribution of the interacting continuum.

The reduced energy $\varepsilon = 2(E - E_{res})/\Gamma$ includes the parameters for the $3s^{-1}4p$ resonance: its linewidth $\Gamma = 76$ meV and energy $E_{res} = 26.6$ eV. The value of the lineshape parameter is $q = -0.25$ and the correlation parameter $\rho^2 = \sigma_a/(\sigma_a + \sigma_b) = 0.89$ [32]. A fit of the numerically-separated H17 lineshape for $J = 3/2$ in figure 3 (791 nm) using these parameters allows the extraction of the width of the spectrometer response function assumed Gaussian. The extracted value of 90 meV full width at half maximum is then used for the simulation of the SBs in the RABBIT spectrogram with equations 6 - 9.

The resonant two-photon transition matrix element for channel (L,ℓ) can be written as [24]:

$$\mathcal{M}_r^{\pm,L,\ell} = M^{(1),L,\ell} \; \frac{q_{\text{eff}}^{\pm,L,\ell} + \varepsilon}{\varepsilon + i} + M^{(2),L,\ell} \quad (11)$$

with the effective complex q parameter [23, 41]:

$$q_{\text{eff}}^{\pm,L,\ell} = q \mp 2(q - i) \; \beta^{L,\ell} \; \hbar\omega_0/\Gamma. \quad (12)$$

$M^{(1),L,\ell}$ and $M^{(2),L,\ell}$ are the two-photon matrix elements associated to the interacting and non-interacting continua. Their values were previously calculated by some of the authors and used in [24]. $q_{\text{eff}}^{\pm,L,\ell}$ includes the dipole-coupling of the intermediate quasi-bound state with the final continuum through the IR field [23, 41] (see red dotted arrows in figure 1). The strength of this process is described by the $\beta^{L,\ell}$ parameter. Figure 6 shows the modulus and phase of $\mathcal{M}_r^{\pm,L,\ell}$ for the three channels when $\beta^{L,\ell}=0$. The channel $L = 2 \; \ell = 3$ is clearly the dominant one, the channel $L = 0 \; \ell = 1$ having a slightly smaller amplitude but a very similar phase. In [24], the best agreement between model and data was found for $\beta^{L,\ell} = 0.005$, which is the value used here for all three channels. The experiment being performed with the reduced 50-nm laser bandwidth, the effects described in Refs [23, 41] arising from short pulses, are not taken into account.

In our analysis, the group delay dispersion of the attosecond pulses (attochirp) [39] is not considered since it only leads to a phase offset. We further assume that the spectral phase of the individual harmonic fields (often referred to as femtochirp) does not vary significantly from one harmonic order to the next. It does not contribute to the phase difference in equation 6. Consequently, the phase of the sideband oscillations in each channel is simply: $\Delta\Phi_a^{\pm,L,\ell}(E) \approx$
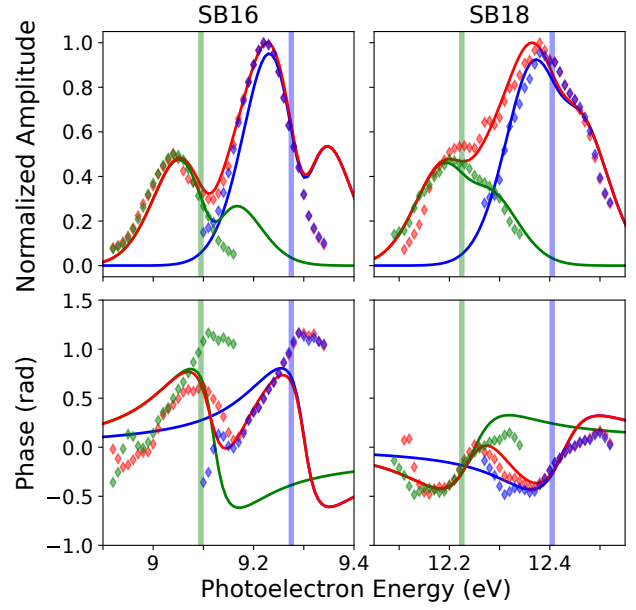

Figure 7: Simulation of the resonant sidebands (solid lines) at $\lambda = 792.3$ nm compared to the experimental data (diamonds). Normalized $2\omega_0$-amplitudes (top panels) and $2\omega_0$-phases (bottom panels) for SB16 and SB18. Green, blue colors are used for the $J = 1/2$, $J = 3/2$ respectively. Red is used for the summed components and measured data. Vertical lines indicate the positions of the resonance shifted up (SB18) or down (SB16) by the energy of one photon energy.

$-\arg[\mathcal{M}_r^{\pm,L,\ell}(E)] + \arg[\mathcal{M}_r^{\pm,L,\ell}(E \rightarrow \infty)]$. Finally, the harmonic spectral amplitude $\mathcal{H}(E)$ is assumed Gaussian and equal for all channels. Its width, determined by comparison with the numerically separated $J = 3/2$ spectrum for SB20 in figure 4(c), is found to be 140 meV full width at half-maximum.

The spectrograms simulated using equation 9 are analyzed like the experimental ones. The amplitudes and phases are shown in figure 7 in red lines for the total and in green and blue lines for the two S-O components. The shape of the amplitude is clearly different in SB16 and SB18. This is due to the different

effective complex parameter $q_{\text{eff}}^{\pm,L,\ell}$ for the two sidebands. The fact that $\beta^{L,\ell}$, although small, is not zero has a strong impact on the two-photon transition complex amplitude. For the same reason, the phase jumps of SB16 are much larger than in SB18.

4. Discussion

Figure 7 shows the comparison between the SB amplitudes and phases from the simulation and the experiment (the data of figure 5 are here plotted as diamonds). The best agreement was found when the simulations were performed for a laser driving wavelength of 792.3 nm. The difference with the experimental value is less than 0.2% which is within the experimental uncertainty. The agreement between the simulated and measured amplitudes (red in figure 7) is remarkable, especially for SB18. A good agreement is also obtained between the measured and simulated total phases (also in red in figure 7), which indicates that the double bumps measured in SB16 and SB18 are signatures of the Fano resonance in the two S-O channels. In particular, the very different modulation amplitudes of the phase jumps measured in SB16 and SB18 are well captured by the simulations. The non-zero β parameter explains the difference with respect to the $2s2p$ resonance in helium (for which $\beta \sim 0$), even though it is not enough to fully recover the exact shapes of the resonant phases, in particular for SB16. A possible reason could be the presence, within SB16, of the $3s^{-1}4s$ two-photon resonance, with $\Gamma = 170$ meV linewidth [42]. Note that the $3s^{-1}4d$ two-photon resonance that could affect SB18 has a linewidth of only $\Gamma = 2$ meV and is thus probably washed out. The simple model used to numerically separate the measured spectrogram in two incoherent contributions
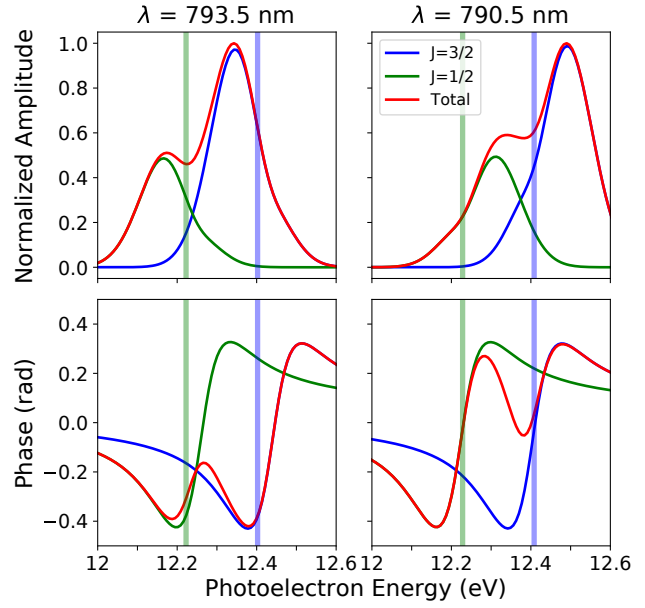

Figure 8: Simulated $2\omega_0$-amplitudes and $2\omega_0$-phases of the total (red), $J = 1/2$ (green) and $J = 3/2$ (blue) contributions of SB18, for different driving laser wavelengths.

also gives quite satisfying results: in SB18, the retrieved amplitudes and phases for each J (green and blue lines and diamonds in figure 7) correspond to a good extent to the results of the simulation. All the above demonstrates the ability of Rainbow RABBIT to distinguish between two nearly-overlapping contributions, here separated only by 177 meV.

The simulations described in section 3 were also used to study the influence of different detunings of the driving laser. The results, presented in figure 8, show significant modifications of both spectral amplitudes and phases. Interestingly, when the resonant harmonic is centered below (above) the resonance, the phase jump corresponding to the $J = 3/2$ ($J = 1/2$) is entirely encoded in the total phase. For instance, when H17 is below the resonance ($\lambda = 793.5$ nm), the total phase (red) fits closely the $J = 3/2$ phase jump (blue) at 12.4 eV. This is due to the fact that

the $J = 1/2$ contribution (green) is very weak at high energy; it plays a role only below $\sim$ 12.3 eV. A combination of measurements with appropriate detunings could reveal differences between the spectral phases of the two S-O components. The experimental realization is though delicate since, to recover the entire phase jump, the phase must be extracted down to 5% of the SB amplitude where the noise level can be important, which was the case for the measurements presented in this work. As shown above, the relatively good agreement of the measured data with our simulations indicates that differences between the two S-O components should be small.

Similarly to what was done for the $2s2p$ resonance in helium [25, 28], we reconstruct the temporal evolution of the EWP emitted through the $3s^{-1}4p$ resonance. The reconstruction of the EWP from experimental data is meaningful when a single channel is dominant or when the main channels present similar dynamics. Otherwise, the incoherent addition of the various channels in the RABBIT spectrogram prevents this reconstruction. Since in figure 6, the $L = 2\ \ell = 3$ channel has the largest amplitude and, furthermore, the second largest channel ($L = 0\ \ell = 1$) has a very similar phase evolution, the dynamics of the former can be recovered. We will compare the temporal evolution of the EWP emitted in the $J = 3/2$ continuum obtained from measurements (figure 9) and from simulations (figure 10) in order to validate these assumptions. The amplitude of the wavepacket is calculated by using the formula reported in the supplementary material of reference [25] as $SB_{18}^{3/2}(E)/\sqrt{2\ SB_{20}^{3/2}(E+2\hbar\omega_0)}$, where $SB_{18}^{3/2}$ and $SB_{20}^{3/2}$ are the experimentally-recovered amplitudes of SB18 and SB20 for the $J = 3/2$ component, respectively. The phase of the

wavepacket is the one experimentally recovered for $J = 3/2$ in SB18. By Fourier transform, we determine the temporal evolution of the two-photon EWP. Note that, in contrast to He, the two-photon EWP is not an exact replica of the resonant one-photon EWP because of the non-zero value of the β parameter in equation 12. It accounts for the possibility of a direct dipole transition from the resonant state to the final continuum, giving rise to an additional two-photon pathway and thus a deviation of the total two-photon EWP from the one-photon EWP. Finite pulse effects, due to the spectral width of the dressing beam ($\sim$50 meV), are expected to play a marginal role, given the broader resonance width (76 meV). The normalized intensity and phase evolution of the EWP are shown in figure 9(a). The intensity variation is essentially a Gaussian profile, with a 12-fs FWHM, centered at time ~ 0 fs. After dropping down to almost zero at time ~ 12 fs, the intensity variation then exhibits a secondary maximum of much smaller amplitude. The strong minimum is accompanied by an abrupt phase jump. This feature is characteristic of the interference between the direct ionisation path and the resonant path. The temporal evolution of the simulated EWP for the channel $L = 2\ \ell = 3$, shown in figure 10(a), reveals a very similar behavior, implying that our assumptions were justified. Nevertheless, the interference position occurs slightly earlier, at ~ 10 fs. Figure 9(b) shows the buildup in time of the (two-photon) resonant spectrum in SB18. This time-frequency representation is obtained by applying a time-limited inverse Fourier transform to the complex EWP as described in [43, 25, 28]. The spectrum is bell-shaped, like the excitation pulse, until ~ 12 fs, then a destructive interference starts to appear at the photoelectron energy of ~ 12.4 eV, digging the window resonance in the pulse spec-
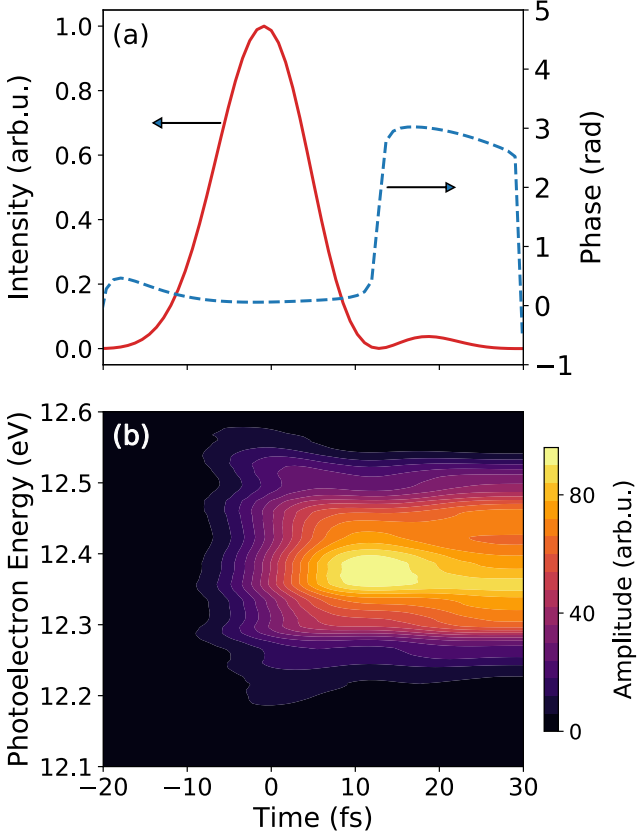
Figure 9: (a) Intensity (red straight line) and phase (blue dashed line) of the temporal reconstruction of the experimental two-photon EWP in SB18 for $J = 3/2$. The arrows indicate the vertical axis corresponding to each curve. (b) Time-frequency representation of the buildup of the corresponding resonant spectrum obtained by time-limited inverse FT. The plots are obtained from experimental data in figure 5 with $\lambda = 791$ nm.
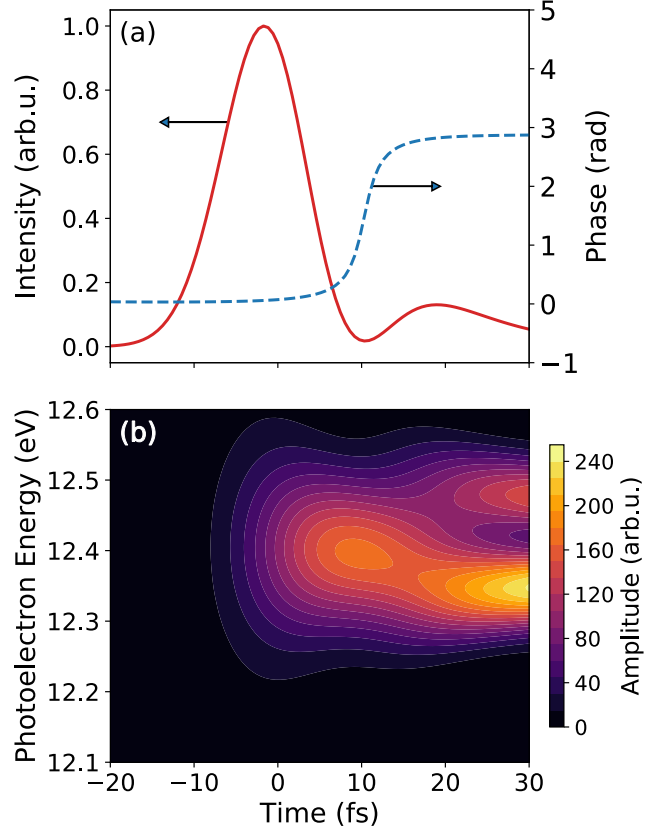
Figure 10: (a) Intensity (red straight line) and phase (blue dashed line) of the temporal reconstruction of the simulated two-photon EWP in SB18 for $J = 3/2$ and for the $L = 2$ $\ell = 3$ channel. (b) Time-frequency representation of the buildup of the corresponding resonant spectrum obtained by time-limited inverse FT. The plots are obtained from simulations for $\lambda = 792.3$ nm without convolution with the spectrometer response function.

trum. This appears even more clearly in the time-frequency representation of the simulated EWP, shown in figure 10(b), where the hole in the spectrum starts to appear at ~ 10 fs. Note that there is very little constructive interference in the buildup because, in contrast to helium, the argon resonance lineshape is quite symmetric.

The position in time of this interference depends on the relative value of the Fourier-

limited duration of the excitation radiation with respect to the resonance lifetime (8 fs). The harmonic width is 140 meV, which corresponds to a Fourier limited duration of 12.8 fs. By increasing the harmonic bandwidth to 280 meV in the simulations, the interference is shifted down to ~ 6 fs.

For comparison, we plot in figure 11 the temporal profile and buildup of the simulated

two-photon EWP in SB16 for the same channel $L = 2$, $\ell = 3$. They are significantly different from those in SB18, with a stronger destructive interference and a higher secondary maximum. Mathematically, this is the result of the change of sign of the complex factor in $q_{\text{eff}}^{\pm}$, see equation 12. This illustrates the importance of the presence of the additional channel involving the direct dipole transition from the resonance to the final continuum that affects differently the sidebands on either side of the resonance.
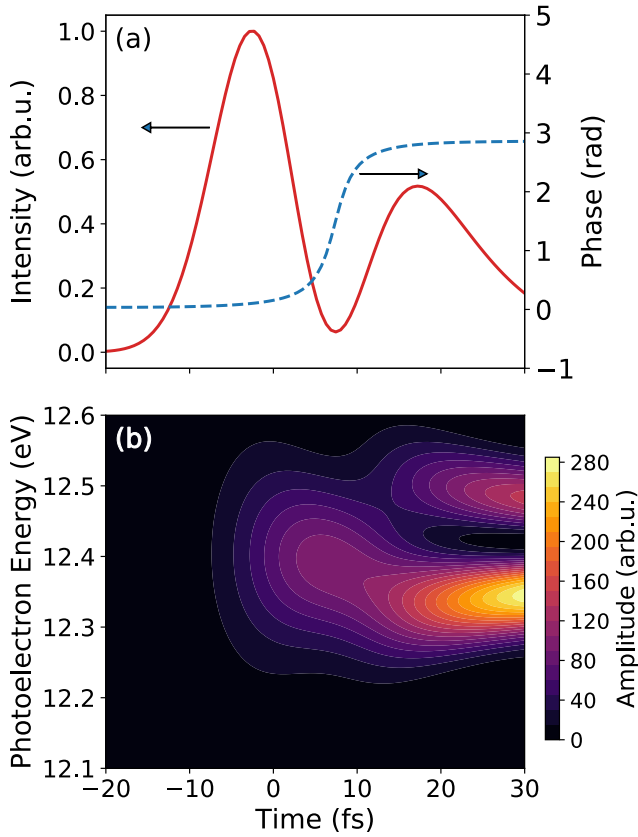

Figure 11: Same as Fig. 10 for SB16.

5. Conclusion

The spectral phase around the $3s^{-1}4p$ Fano resonance in argon has been measured for photoionization leaving the Ar^+ ion in two different spin-orbit states. We show that

a spectrally-resolved electron interferometry technique, the Rainbow RABBIT, is able to distinguish between the two nearly-overlapping S-O contributions, here separated only by 177 meV. Assuming identical resonant transitions for the two S-O components, a simple model is used to numerically separate the measured spectrograms in the two incoherent contributions. The comparison with simulations based on the same assumption gives quite satisfying results. The double signature of the resonance is recovered in both amplitude and phase and attributed to the two S-O components. The simulations also explain the very different amplitude of the phase jumps measured in the lower and upper sidebands with respect to the resonant harmonic. Our approach intrinsically yields identical results for the two fine-structure states. A better theoretical description could be obtained by adding relativistic effects [44, 45]. Finally, a more complete description of the photoionization process, including coherence between multiple ionization channels, could be measured using the Mixed-FROG approach [46, 47].

Acknowledgments

References

[1] Krausz F and Ivanov M 2009 *Rev. Mod. Phys.* **81**(1) 163–234 URL https://link.aps.org/

doi/10.1103/RevModPhys.81.163

[2] Schultze M, Fieß M, Karpowicz N, Gagnon J, Korbman M, Hofstetter M, Neppl S, Cavalieri A L, Komninos Y, Mercouris T, Nicolaides C A, Pazourek R, Nagele S, Feist J, Burgdörfer J, Azzeer A M, Ernstorfer R, Kienberger R, Kleineberg U, Goulielmakis E, Krausz F and Yakovlev V S 2010 *Science* **328** 1658–1662 ISSN 0036-8075 (*Preprint* http://science.sciencemag.org/content/328/5986/1658.full.pdf) URL http://science.sciencemag.org/content/328/5986/1658

[3] Klünder K, Dahlström J M, Gisselbrecht M, Fordell T, Swoboda M, Guénot D, Johnsson P, Caillat J, Mauritsson J, Maquet A, Taïeb R and L'Huillier A 2011 *Phys. Rev. Lett.* **106**(14) 143002 URL https://link.aps.org/doi/10.1103/PhysRevLett.106.143002

[4] Palatchi C, Dahlström J M, Kheifets A, Ivanov I, Canaday D, Agostini P and DiMauro L 2014 *Journal of Physics B: Atomic, Molecular and Optical Physics* **47** 245003

[5] Isinger M *et al.* 2017 *Science* **358** 893 ISSN 0036-8075 (*Preprint* http://science.sciencemag.org/content/358/6365/893.full.pdf) URL http://science.sciencemag.org/content/358/6365/893

[6] Haessler S, Fabre B, Higuet J, Caillat J, Ruchon T, Breger P, Carré B, Constant E, Maquet A, Mével E, Salières P, Taïeb R and Mairesse Y 2009 *Phys. Rev. A* **80** ISSN 1050-2947

[7] Caillat J, Maquet A, Haessler S, Fabre B, Ruchon T, Salieres P, Mairesse Y and Taïeb R 2011 *Physical review letters* **106** 093002

[8] Huppert M, Jordan I, Baykusheva D, von Conta A and Wörner H J 2016 *Phys. Rev. Lett.* **117**(9) 093001 URL https://link.aps.org/doi/10.1103/PhysRevLett.117.093001

[9] Beaulieu S, Comby A, Clergerie A, Caillat J, Descamps D, Dudovich N, Fabre B, Géneaux R, Légaré F, Petit S *et al.* 2017 *Science* **358** 1288–1294

[10] Vos J, Cattaneo L, Patchkovskii S, Zimmermann T, Cirelli C, Lucchini M, Kheifets A, Landsman A and Keller U 2018 *Science* **360** 1326–1330

[11] Nandi S, Plésiat E, Zhong S, Palacios A, Busto D, Isinger M, Neoričić L, Arnold C, Squibb R, Feifel R *et al.* 2019 *arXiv preprint arXiv:1911.08181*

[12] Cavalieri A L, Müller N, Uphues T, Yakovlev V S, Baltuska A, Horvath B, Schmidt B, Blümel L, Holzwarth R, Hendel S, Drescher M, Kleineberg U, Echenique P M, Kienberger R, Krausz F and Heinzmann U 2007 *Nature* **449** 1029 EP – URL https://doi.org/10.1038/nature06229

[13] Locher R, Castiglioni L, Lucchini M, Greif M, Gallmann L, Osterwalder J, Hengsberger M and Keller U 2015 *Optica* **2** 405–410 URL http://www.osapublishing.org/optica/abstract.cfm?URI=optica-2-5-405

[14] Tao Z, Chen C, Szilvási T, Keller M, Mavrikakis M, Kapteyn H and Murnane M 2016 *Science* **353** 62–67

[15] Dahlström J, L'Huillier A and Maquet A 2012 *Journal of Physics B: Atomic, Molecular and Optical Physics* **45** 183001

[16] Maquet A, Caillat J and Taïeb R 2014 *Journal of Physics B: Atomic, Molecular and Optical Physics* **47** 204004 URL https://doi.org/10.1088%2F0953-4075%2F47%2F20%2F204004

[17] Pazourek R, Nagele S and Burgdörfer J 2015 *Rev. Mod. Phys.* **87**(3) 765–802 URL https://link.aps.org/doi/10.1103/RevModPhys.87.765

[18] Itatani J, Quéré F, Yudin G L, Ivanov M Y, Krausz F and Corkum P B 2002 *Phys. Rev. Lett.* **88**(17) 173903 URL https://link.aps.org/doi/10.1103/PhysRevLett.88.173903

[19] Kienberger R, Goulielmakis E, Uiberacker M, Baltuska A, Yakovlev V, Bammer F, Scrinzi A, Westerwalbesloh T, Kleineberg U, Heinzmann U *et al.* 2004 *Nature* **427** 817–821

[20] Paul P, Toma E, Breger P, Mullot G, Augé F, Balcou P, Muller H and Agostini P 2001 *Science* **292** 1689–1692

[21] Muller H G 2002 *Applied Physics B* **74** s17–s21

[22] Jordan I, Huppert M, Pabst S, Kheifets A S, Baykusheva D and Wörner H J 2017 *Physical Review A* **95** 1–7 ISSN 24699934

[23] Jiménez-Galán A, Argenti L and Martín F 2014 *Phys. Rev. Lett.* **113**(26) 263001 URL https://link.aps.org/doi/10.1103/PhysRevLett.113.263001

[24] Kotur M, Guénot D, Jiménez-Galán, Kroon D, Larsen E W, Louisy M, Bengtsson S, Miranda M, Mauritsson J, Arnold C L, Canton S E, Gisselbrecht M, Carette T, Dahlström J M, Lindroth E, Maquet A, Argenti L, Martín F and L'Huillier A 2016 *Nature Communications* **7** 1–6 ISSN 20411723 (*Preprint* 1505.02024)

[25] Gruson V, Barreau L, Jiménez-Galan, Risoud F, Caillat J, Maquet A, Carré B, Lepetit F,

Hergott J F, Ruchon T, Argenti L, Taïeb R, Martín F and Salières P 2016 *Science* **354** 734–738 ISSN 10959203

[26] Argenti L, Jiménez-Galán A, Caillat J, Taïeb R, Maquet A and Martín F 2017 *Phys. Rev. A* **95**(4) 043426 URL https://link.aps.org/doi/10.1103/PhysRevA.95.043426

[27] Cirelli C, Marante C, Heuser S, Petersson C L M, Galán Á J, Argenti L, Zhong S, Busto D, Isinger M, Nandi S, Maclot S, Rading L, Johnsson P, Gisselbrecht M, Lucchini M, Gallmann L, Dahlström J M, Lindroth E, L'Huillier A, Martín F and Keller U 2018 *Nature Communications* **9** 955 ISSN 2041-1723 URL https://doi.org/10.1038/s41467-018-03009-1

[28] Busto D, Barreau L, Isinger M, Turconi M, Alexandridi C, Harth A, Zhong S, Squibb R J, Kroon D, Plogmaker S, Miranda M, Jiménez-Galán Á, Argenti L, Arnold C L, Feifel R, Martín F, Gisselbrecht M, L'Huillier A and Salières P 2018 *Journal of Physics B: Atomic, Molecular and Optical Physics* **51** 044002 URL https://doi.org/10.1088%2F1361-6455%2Faaa057

[29] Barreau L, Petersson C L M, Klinker M, Camper A, Marante C, Gorman T, Kiesewetter D, Argenti L, Agostini P, González-Vázquez J, Salières P, DiMauro L F and Martín F 2019 *Phys. Rev. Lett.* **122**(25) 253203 URL https://link.aps.org/doi/10.1103/PhysRevLett.122.253203

[30] Beutler H 1935 *Zeitschrift für Physik* **93** 177–196

[31] Fano U 1961 *Physical Review* **124** 1866–1878 ISSN 0031899X (*Preprint* 0611602)

[32] Sorensen S L, Åberg T, Tulkki J, Rachlew-Källne E, Sundström G and Kirm M 1994 *Phys. Rev. A* **50**(2) 1218–1230 URL https://link.aps.org/doi/10.1103/PhysRevA.50.1218

[33] Berrah N, Langer B, Bozek J, Gorczyca T W, Hemmers O, Lindle D W and Toader O 1996 *Journal of Physics B: Atomic, Molecular and Optical Physics* **29** 5351–5365

[34] Yamada C, Kanamori H and Hirota E 1985 *The Journal of Chemical Physics* **83** 552–555 (*Preprint* https://doi.org/10.1063/1.449520) URL https://doi.org/10.1063/1.449520

[35] Kroon D, Guénot D, Kotur M, Balogh E, Larsen E W, Heyl C M, Miranda M, Gisselbrecht M, Mauritsson J, Johnsson P, Varjú K,

L'Huillier A and Arnold C L 2014 *Opt. Lett.* **39** 2218–2221 URL http://ol.osa.org/abstract.cfm?URI=ol-39-7-2218

[36] Zürch M, Chang H T, Borja L J, Kraus P M, Cushing S K, Gandman A, Kaplan C J, Oh M H, Prell J S, Prendergast D, Pemmaraju C D, Neumark D M and Leone S R 2017 *Nature Communications* **8** ISSN 20411723 (*Preprint* 1702.03822)

[37] Canton-Rogan S E, Wills A A, Gorczyca T W, Wiedenhoeft M, Nayandin O, Liu C N and Berrah N 2000 *Phys. Rev. Lett.* **85**(15) 3113–3116 URL https://link.aps.org/doi/10.1103/PhysRevLett.85.3113

[38] Denise Caldwell C, Whitfield S and Krause M 2000 *Molecular Physics* **98** 1075–1082

[39] Mairesse Y, De Bohan A, Frasinski L, Merdji H, Dinu L, Monchicourt P, Breger P, Kovačev M, Taïeb R, Carré B, Muller H, P A and P S 2003 *Science* **302** 1540–1543

[40] Fano U and Cooper J W 1965 *Phys. Rev.* **137**(5A) A1364–A1379 URL https://link.aps.org/doi/10.1103/PhysRev.137.A1364

[41] Jiménez-Galán A, Martín F and Argenti L 2016 *Physical Review A* **93** 1–21 ISSN 24699934 (*Preprint* 1509.05814)

[42] Mitchell P, Baxter J A, Comer J and Hicks P J 1980 *Journal of Physics B: Atomic and Molecular Physics* **13** 4481–4494 URL https://doi.org/10.1088%2F0022-3700%2F13%2F22%2F020

[43] Wickenhauser M, Burgdörfer J, Krausz F and Drescher M 2005 *Phys. Rev. Lett.* **94**(2) 023002 URL https://link.aps.org/doi/10.1103/PhysRevLett.94.023002

[44] Saha S, Mandal A, Jose J, Varma H R, Deshmukh P C, Kheifets A S, Dolmatov V K and Manson S T 2014 *Phys. Rev. A* **90**(5) 053406 URL https://link.aps.org/doi/10.1103/PhysRevA.90.053406

[45] Kheifets A, Mandal A, Deshmukh P C, Dolmatov V K, Keating D A and Manson S T 2016 *Phys. Rev. A* **94**(1) 013423 URL https://link.aps.org/doi/10.1103/PhysRevA.94.013423

[46] Bourassin-Bouchet C and Couprie M E 2015 *Nature communications* **6** 1–7

[47] Bourassin-Bouchet C, Barreau L, Gruson V, Hergott J F, Quéré F, Salières P and Ruchon T (accepted) *Phys. Rev. X*